The Astrophysical Journal, 682:1328–1337, 2008 August 1
© 2008. The American Astronomical Society. All rights reserved. Printed in U.S.A.

VALIDATION OF TWO MHD MODELS OF THE SOLAR CORONA WITH ROTATIONAL TOMOGRAPHY

Alberto M. Vásquez
Instituto de Astronomía y Física del Espacio, CONICET-University of Buenos Aires, Ciudad de Buenos Aires, CC 67-Suc 28, Argentina; albert@iafe.uba.ar

Richard A. Frazin
Department of Ocean, Atmospheric and Space Science, University of Michigan, Ann Arbor, MI 48109; rfrazin@umich.edu

Keiji Hayashi
W. W. Hansen Experimental Physics Laboratory, Stanford University, Stanford, CA 94305

Igor V. Sokolov, Ofer Cohen, and Ward B. Manchester IV
Department of Ocean, Atmospheric and Space Science, University of Michigan, Ann Arbor, MI 48109

and

Farzad Kamalabadi
Department of Electrical and Computer Engineering, University of Illinois, Urbana, IL 61801
Received 2007 December 19; accepted 2008 April 8

ABSTRACT

We demonstrate a validation of two 3D MHD models of the corona by comparing density values from solar rotational tomography (SRT) to densities and morphological properties of the two MHD solutions for CR 2029 (2005 April 21–May 18). The two MHD models are given by the Stanford and Michigan models, and both use the same synoptic magnetogram from MDI as a lower boundary condition. The SRT reconstructions are based on polarized white-light images MLSO Mk IV data for the region between 1.1 and 1.5 $R_\odot$ (solar radii) and LASCO C2 for the region between 2.3 and 6.0 $R_\odot$. While the Stanford MHD model reasonably reproduces the tomographic density over the south pole, it fares less well over the north pole, and the Michigan MHD model underestimates the density over both poles. At lower latitudes, we find that while the MHD models have better agreement with the tomographic densities in the region below 3.5 $R_\odot$, at larger heights the agreement is more problematic. Our interpretation is that the base densities and temperatures of the models need to be improved, as well as their radial density gradients.

Subject headings: methods: numerical — solar wind — Sun: corona — Sun: magnetic fields — techniques: image processing

Online material: color figures

1. INTRODUCTION

Three-dimensional (3D) magnetohydrodynamics (MHD) models of the corona are required for space weather forecasting and for understanding the basic physics of coronal mass ejection (CME) propagation and the quasi-steady solar wind. The ability of these models to accurately model the density is fundamental to our knowledge of the dynamical processes that occur in the solar corona and the heliosphere. The works of Odstrcil & Pizzo (1999) and Mancuso & Raymond (2004) have shown that CMEs have very significant interactions with streamer belt structures. In particular, the density of the corona strongly affects the propagation of CMEs (Riley et al. 2001; Odstrcil et al. 2002; Manchester et al. 2004), as it determines the amount of plasma swept up by the CME and its acceleration (Lugaz et al. 2005). The density is also important for calculating the Alfvén Mach number and compression ratio of CME-driven shocks, which, in turn, determines the energy spectra of energetic particles (Reames 1999; Sokolov 2004; Manchester et al. 2005).

In this work, we chose Carrington rotation 2029 (CR 2029; starting 2005 April 21.3, ending 2005 May 18.6) to compare the electron density (N_e) predictions and the magnetic field morphologies of the Stanford and Michigan MHD models to the densities determined from the solar rotational tomography (SRT) technique. Figure 1 shows an 2005 April 30th composite image of the solar corona using the normalizing-radial-graded filter (NRGF) method (Morgan et al. 2006). The coronal image is composed of independent images from EIT 304, Mk IV (daily average), and LASCO C2 out to 4 $R_\odot$. CR 2029 includes the 2005 May 13th SHINE campaign event, which was full-halo CME observed by LASCO C2 starting at 17:22 UT. (Note that any frame including a CME is removed before SRT processing.) *GOES* reported a long-duration two-ribbon M8.0 X-ray flare on NOAA Active Region (AR) 10759 (with coordinates N12° E11°) between 16:13 and 17:28 UT with peak emission at 16:57 UT. Also, EIT 195 images show a strong brightening that starts to develop at 16:37 UT. The interest in this event is due to the fact that it was observed in all its stages by many different instruments (both remotely and in situ) on diverse spacecraft (*RHESSI*, *TRACE*, *SOHO*, *ACE*). We refer the reader to the work by Yurchyshyn et al. (2006) for a detailed study of the 2005 May 13th eruption, the resulting CME, and its associated interplanetary manifestation.

SRT was first performed by Altschuler & Perry (1972), and subsequent work has been reviewed by Frazin (2000) and Frazin & Janzen (2002). In the latter work, a cylindrical grid was used to perform the tomographic inversions. Frazin et al. (2007b) introduced a new spherical grid and analyzed the effect of image cadence on the reconstructions. The SRT reconstructions here are based on polarized white-light images Mauna Loa Solar Observatory (MLSO) Mk IV data for the region between 1.1 and 1.5 $R_\odot$ and Large Angle and Spectrometric Coronagraph Experiment (LASCO) C2 for the region between 2.3 and 6.0 $R_\odot$. These

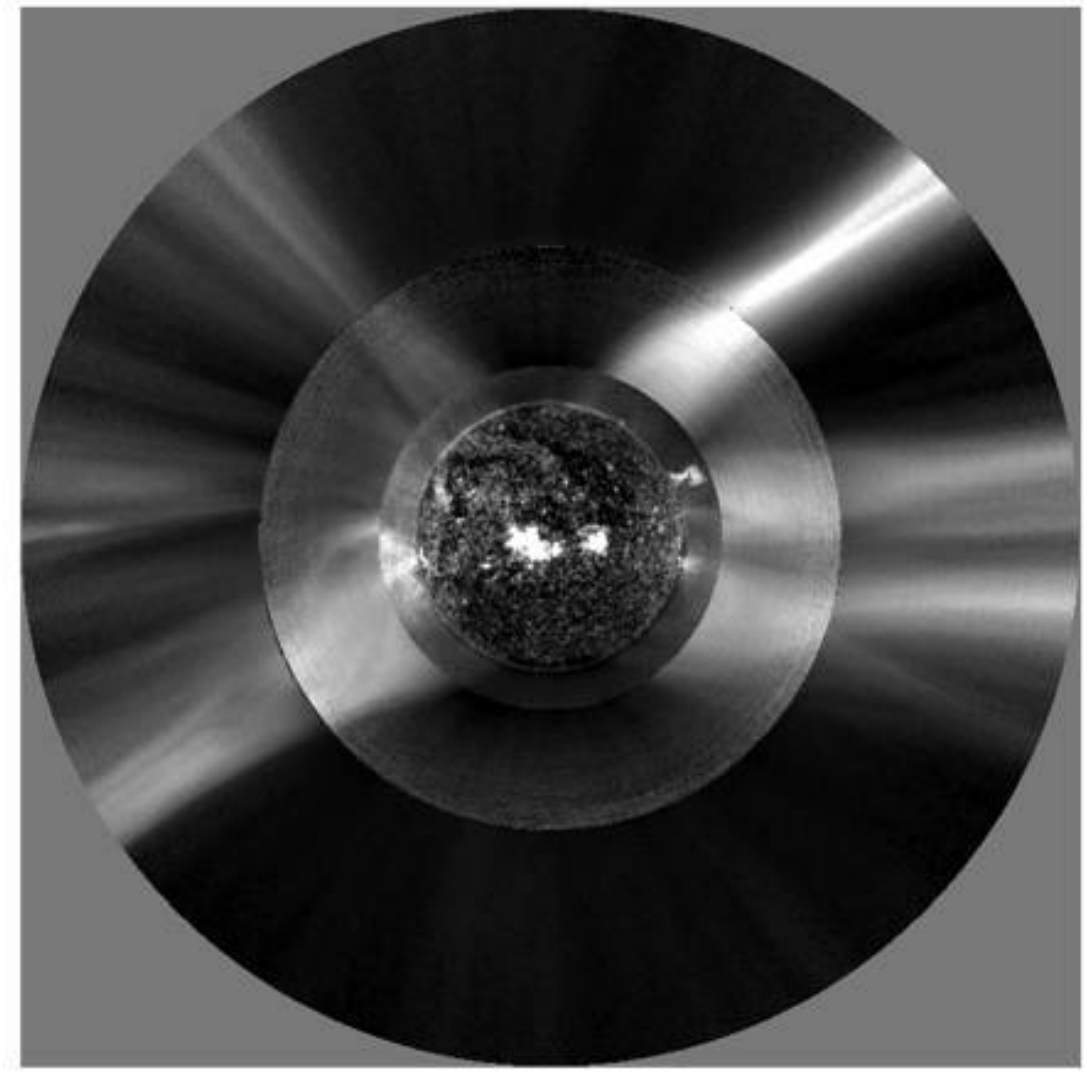

FIG. 1.—2005 April 30th composite image of the solar corona, during the period analyzed in this paper. The coronal image is composed of independent images from EIT 304, Mk IV (daily average), and LASCO C2 out to 4 $R_\odot$.

reconstructed regions are smaller than the instrument fields of view due to edge effects and noise. The spherical grid used to analyze the Mk IV data consists of $35 \times 60 \times 120$ (radial $\times$ latitudinal $\times$ longitudinal) bins. The radial and angular resolutions are about 0.05 $R_\odot$ and 3°, respectively. The spherical grid used to analyze the LASCO data consists of $40 \times 60 \times 120$ (radial $\times$ latitudinal $\times$ longitudinal) bins. The radial and angular resolutions are about 0.1 $R_\odot$ and 3°, respectively. In the case of MLSO Mk IV we used data for the 14 day data set in the period 2005.0505–2005.0519 (consisting of 13 images). In the case of LASCO C2, we performed reconstructions for the 14 day period 2005.0514–2005.0527 (consisting of 16 images).

Both the Michigan and Stanford models are initialized with potential field source surface (PFSS) magnetic models (with a source surface at 2.5 $R_\odot$), with the lower boundary condition prescribed by the Michelson Doppler Imager (MDI) line-of-sight magnetogram for CR 2029. Both models use time-dependent MHD and are run to a steady state, using the same MDI magnetogram as the magnetic boundary condition for the MHD phase of modeling process. The Stanford model PFSS extrapolation was computed up to the order $N = 9$ in the spherical harmonics polynomials, while the Michigan model was computed up to the order $N = 90$.

The Stanford model uses a new boundary formulation at the solar corona base to treat the nonlinear MHD interactions between the solar surface and the corona. We refer the reader to the work by Hayashi (2005, and references therein) for full details on the model, and where different boundary conditions are explored. The model assumes a fully polytropic adiabatic expansion and, in the present work, the same value for the polytropic index ($\gamma = 1.05$) is set at the solar surface and throughout the corona's volume. The model uses a spherical computational grid, with a uniform resolution in the angular directions (of about 3°), and a non-uniform one in the radial direction (ranging from about 0.01 $R_\odot$ at the coronal base to about 0.1 $R_\odot$ at heliospheric height 5.0 $R_\odot$).

The Michigan model (Cohen et al. 2007a, 2007b) assumes a gas with a spatially variable polytropic index. It incorporates the Wang-Sheeley-Arge (WSA) model (Arge et al. 2003, 2004) to relate the terminal wind speed along each magnetic field line to its geometrical expansion factor. The WSA model is an improved version of the original model by Wang & Sheeley (1990). After the PFSS model is obtained, the terminal wind speed is calculated for each magnetic field line. As the Bernoulli integral is constant along each field line (Cohen et al. 2007a, 2007b), one can relate the terminal wind speed to the specific enthalpy at the field

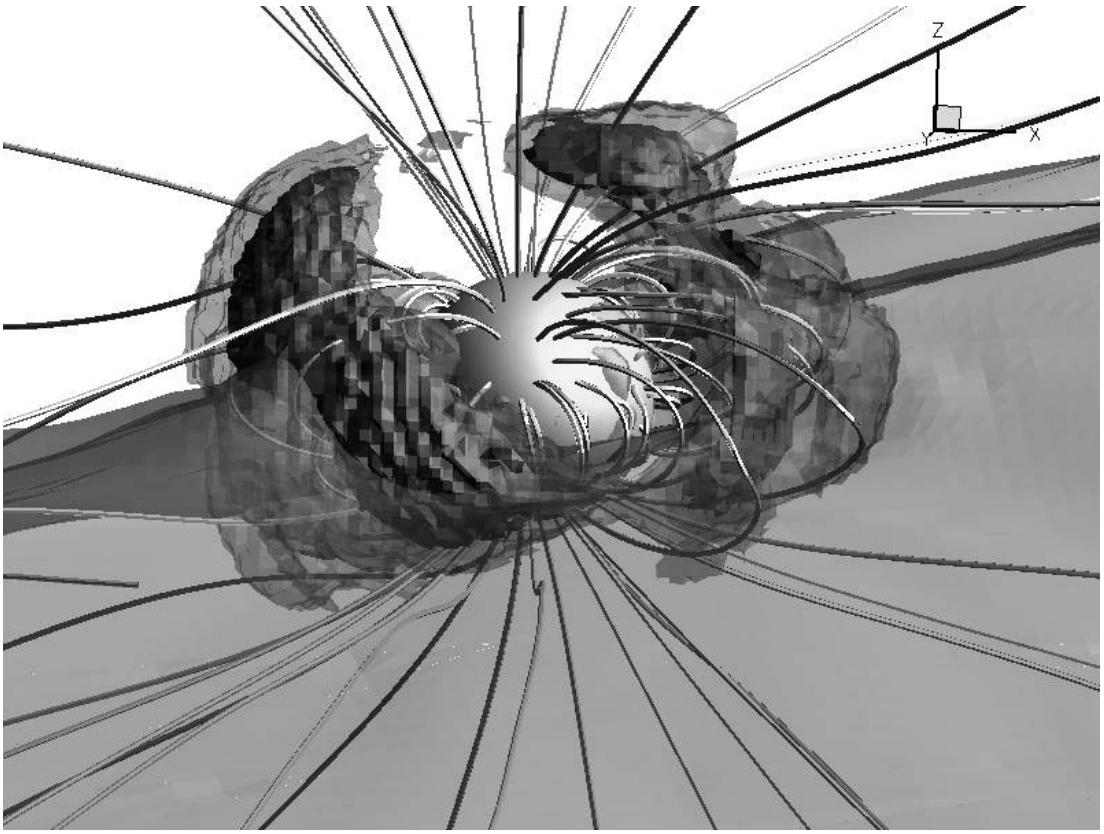

FIG. 2.— A 3D view of combined results for CR 2029. The Sun surface is indicated in yellow. Various field lines from the Michigan MHD model are shown in black and white, and the green surface is the neutral sheet. Overplotted we show two isosurfaces of the SRT reconstructed densities corresponding to the values 10^6 cm^{-3} (*solid red*) and 5×10^5 cm^{-3} (*translucent blue*). [*See the electronic edition of the Journal for a color version of this figure.*]

line footpoint. Once the base temperature at the footnote point is specified (the base temperature is a free parameter), the polytropic index value for this point can be determined from the specific enthalpy. By interpolating along field lines between thus defined values at the surface and a constant value at the source surface, the polytropic index, γ is found throughout the coronal structure (but only on open field lines). Thus, the model involves the phenomenological parametric modeling of the heating through a varied polytropic index instead of the widely used approach of direct specification of volumetric heating functions. Once the model is initialized with PFSS model and the γ is determined, the MHD code is run until a steady state is achieved. The MHD code uses a non-uniform block adaptive Cartesian grid. The grid refinement is interactively implemented throughout the simulation to achieve the necessary resolution within the cells in which the magnetic field lines flip their polarity. This is typically applied around active regions (reaching a grid cell size of 0.02 $R_\odot$ on the solar surface), and also to treat the current sheet (where a grid size of 0.2 $R_\odot$ is typically used); see Cohen et al. (2007a).

2. RESULTS

Figure 2 shows a 3D view of SRT and MHD modeling combined results for CR 2029. The Sun's surface is indicated in yellow. The black and white shaded field lines are selected from the Michigan MHD model, for which we also show the neutral sheet (indicated in green). The figure shows two isosurfaces of the SRT reconstructed densities, corresponding to the values 10^6 cm^{-3} (indicated by solid dark red) and 5×10^5 cm^{-3} (indicated by translucent blue). At heliospheric heights near 2 $R_\odot$, the red isosurface closely follows the streamer belt closed magnetic field lines arising from the MHD model. At larger heights, the blue surface contains plasma that is around the closed structures (streamer legs) or right above the streamers' cusp regions. Note that the density isosurfaces do not close because this reconstruction does not go below 2.3 $R_\odot$.

Figures 3 and 4 show the results from the SRT reconstructions and both of the MHD models at three selected heliocentric heights: 1.25, 2.55, and 4.50 $R_\odot$. Both figures contain the same SRT electron density (N_e) maps, with the value of N_e in units of cm^{-3} indicated by the color bar. The black contours in Figure 3 show the MHD model values of the radial magnetic field (in Gauss), as well the neutral line, while those in Figure 4 show the values of N_e from the MHD models. In both Figures 3 and 4 the Stanford and Michigan models results are displayed on the left and right, respectively. The SRT reconstructions exhibit dark regions called zero-density artifacts (ZDAs). These are artifacts of the reconstruction that are likely to be caused by coronal dynamics (Frazin & Janzen 2002; Frazin & Kamalabadi 2005; Frazin et al. 2007b), which are not taken into account in the tomographic inversion process (although see Frazin et al. 2005a).

The first striking characteristic in all the panels of Figure 3 is that the magnetic neutral line (the thick line) passes near the SRT density maxima corresponding to the streamer belt region. At 1.25 $R_\odot$, covered by the Mk IV reconstruction, the MHD models show complex structure due to the closed field regions. The magnetic neutral line overlies the enhanced density streamer belt in both models. At the heights covered by the LASCO C2 reconstruction (2.55 and 4.50 $R_\odot$), the morphology of the neutral line of the two models is very similar, although they display some differences. First, the Michigan neutral line follows the peak density of the streamer belt as seen from SRT more closely. This is most easily seen at the highest density region of the streamer belt

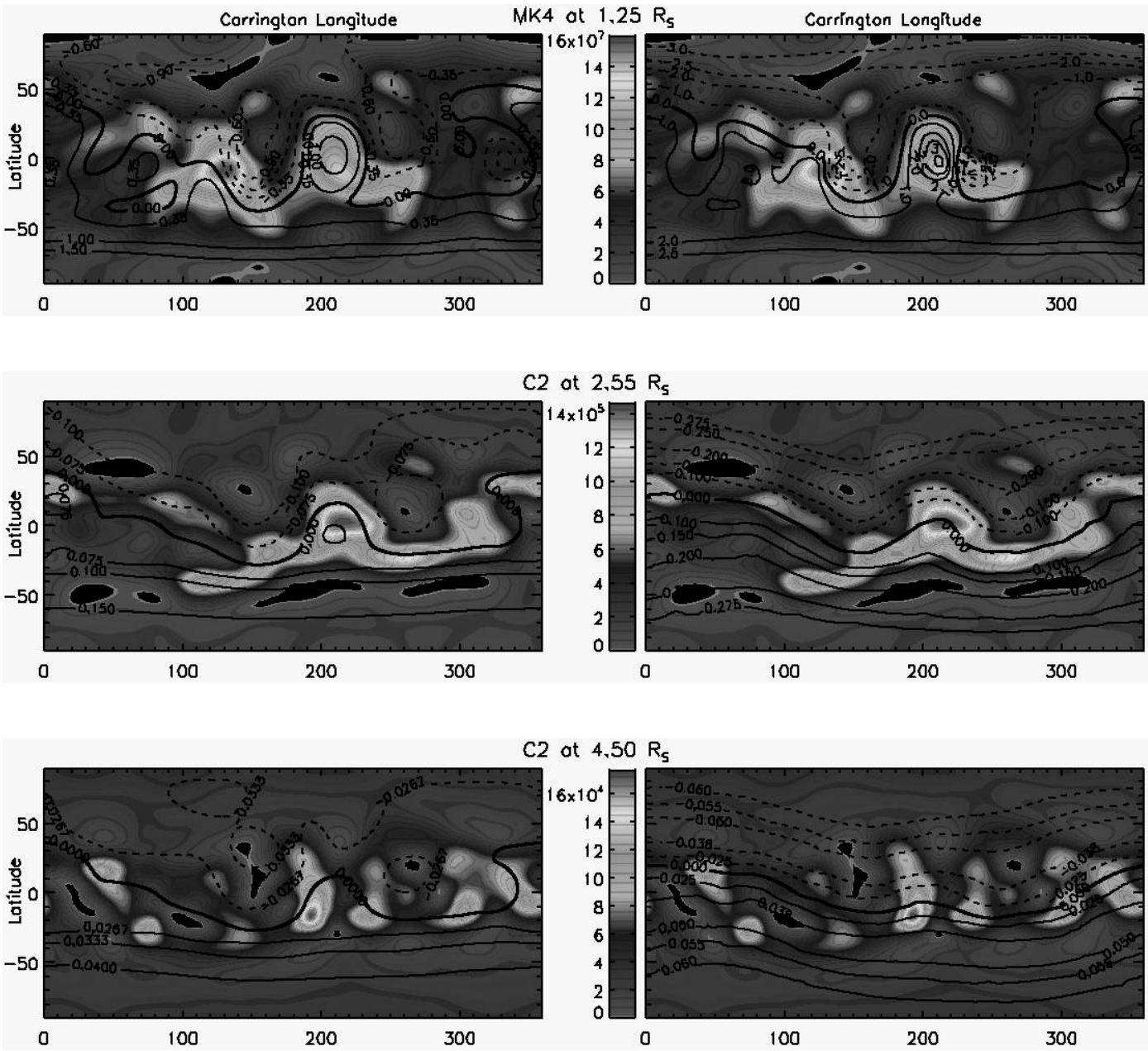

FIG. 3.— Comparison of the tomographic reconstructed 3D coronal electron density (color maps) and the MHD model radial magnetic strength (black contours, labeled in units of Gauss) at three selected heights. The solid thick line indicates the neutral line and the solid (dashed) thin lines indicate positive (negative) values. *Left*: Stanford model contour levels. *Right*: Michigan model contour levels. [*See the electronic edition of the Journal for a color version of this figure*.]

at 2.55 $R_\odot$, near the equator. Second, at higher latitudes, the magnetic models show differences both in scale and morphology. The Michigan model does not have the twisted magnetic structure that the Stanford model neutral line shows north of the neutral line in the longitude range (300°,360°) in the C2 height range. This structure better reflects the underlying enhanced density region at those longitudes (seen in the SRT), for example at 2.55 $R_\odot$. There are other examples of the Stanford model that better reflect streamer shapes seen in the tomography, at heights not included in the figures shown here.

We turn our attention to the density comparison displayed in Figure 4. We first focus on the streamer-subpolar region density contrast structure seen in the SRT reconstructions, where the color maps change from deep blue to violet. Both models are reasonably consistent with this transition and the polar densities at 1.25 $R_\odot$; however, at larger heights the model agreement is less clear. As an example, at 4.50 $R_\odot$ the Stanford model overestimates the tomographic subpolar densities by a factor of order 3, while the Michigan model underestimates them by a factor of order 5. As for the accuracy of the tomographic densities at high latitudes, they depend on the coronagraphs being able to accurately measure the coronal pB above the poles, which is difficult due to the low signal level and polarized stray light issues. The Mk IV polar pB values tend to get lost in the noise at about 1.8 $R_\odot$ (for Mk IV calibration see Elmore et al. 2003). The polar pB values measured by LASCO should be accurate as well, although the C2 polar pB values exhibit a ~40% difference between north and south that was not seen by the well-characterized Ultraviolet Coronagraph Spectrometer (UVCS) White Light Channel in an extensive intercalibration study (Frazin et al. 2002; see also Moran et al. 2006). We further discuss polar densities below, in reference to Figure 9. The tomographic inversion of the polar regions should

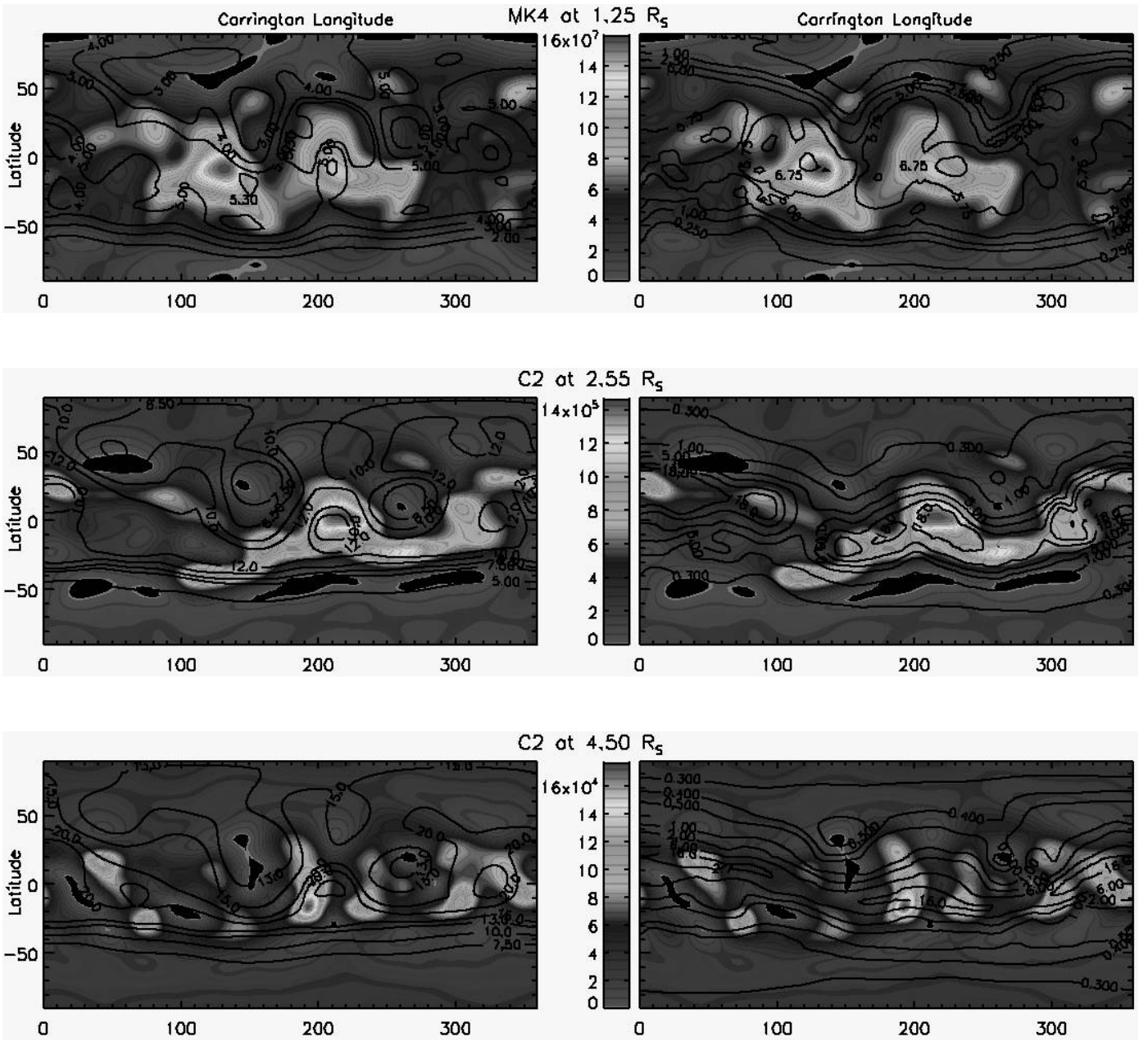

FIG. 4.—Comparison of the tomographic reconstructed 3D coronal electron density (color maps) and the MHD model densities (black contour levels, in same units as color maps) at three selected heights. *Left*: Stanford model contour levels. *Right*: Michigan model contour levels. [*See the electronic edition of the Journal for a color version of this figure.*]

be accurate as well since the dynamics play a less prominent role than in the streamer belt.

We make the following comparison at the streamer belt density peaks of the SRT maps seen in Figures 3 and 4. In the lower height range, covered by Mk IV, the MHD models exhibit lower densities than those of the tomographic reconstruction. At 1.25 $R_\odot$, the Stanford model density values peak at about 35% of the values of the SRT densities. At that same height, the Michigan density values peak at about 50% of the values of the SRT densities. In the higher height range, covered by LASCO C2, both models exhibit higher densities than the tomographic values. At 2.55 $R_\odot$, the Stanford model density values peak at similar or 25% higher values than the SRT reconstructed densities, while showing values up to twice those of the tomography at 4.50 $R_\odot$. At 2.55 $R_\odot$, the Michigan model density values peak about 25%–50% above the values of the SRT reconstructed densities, while showing values comparable to the tomographic ones at 4.50 $R_\odot$. Both MHD models have trouble reproducing the dynamic range seen in the streamer belt tomographic reconstruction at 1.25 $R_\odot$, although the Michigan model does somewhat better in this regard. In both cases, the lack of dynamic range at these lower heights points to the need to improve the treatment of closed field regions.

If we look at the smaller scale structures within the streamer belt, we find that both models are capable of reproducing some of them, especially at heights around 2.55 $R_\odot$. This is the case, for example, of the highest density feature around (0°,210°) at 2.55 $R_\odot$. Similarly, both models are able to closely match the location of other enhanced density features of the SRT density maps. Some examples, closely matched by one or both models, are those around (0°,130°) and (0°,220°) at 1.25 $R_\odot$, and (25°,10°),

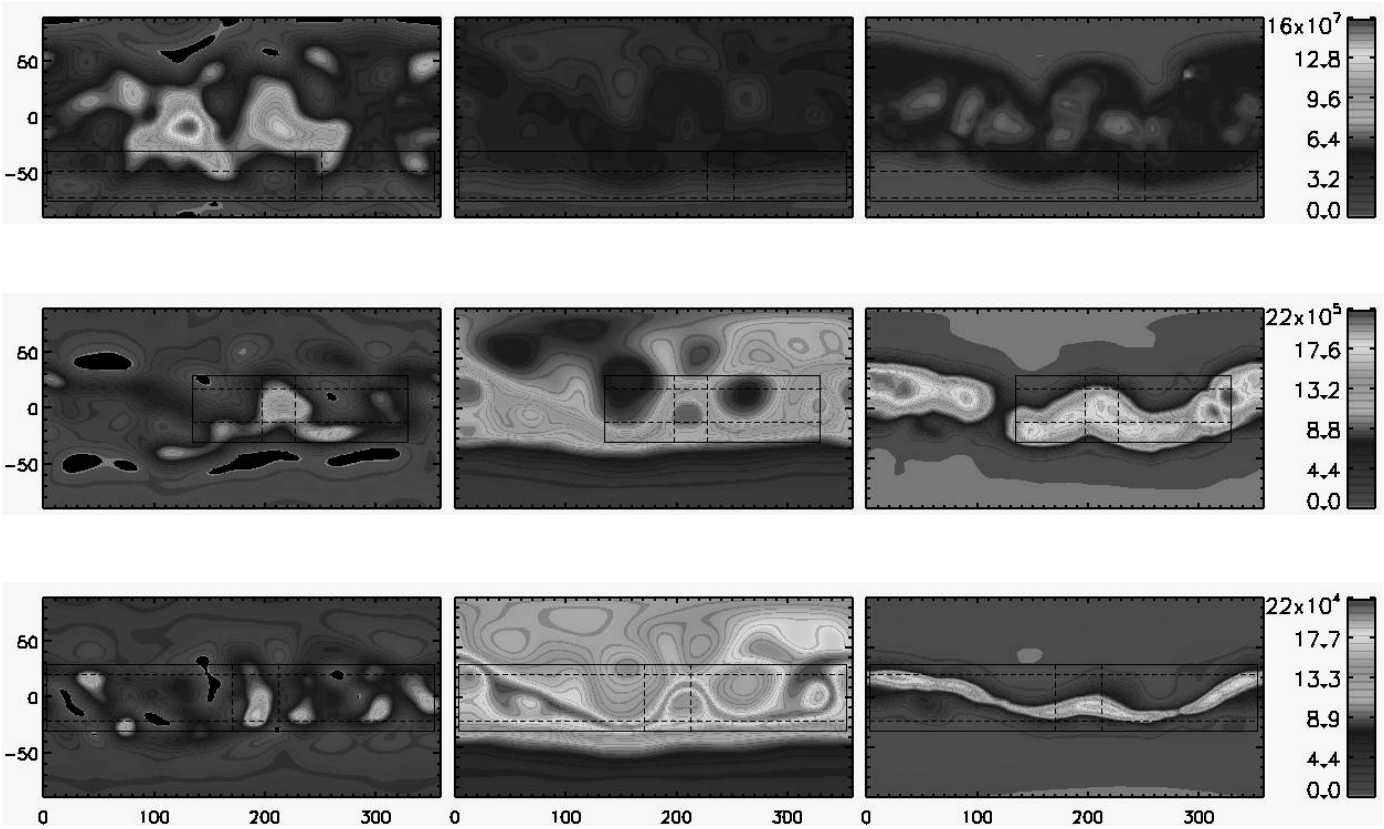

FIG. 5.—Electron density color maps from the tomographic reconstruction (*right*), Stanford model (*middle*), and Michigan model (*left*). The top row of panels corresponds to 1.25 $R_\odot$, the middle row to 2.55 $R_\odot$ and the bottom row to 4.50 $R_\odot$. At each height (*rows*) the color scale is common through the three models (*columns*), with the color bars indicating electron density values in cm^{-3}. At the different heights, the regions bounded by solid and dashed lines are used for the analysis presented in Figs. 6–8. [*See the electronic edition of the Journal for a color version of this figure*.]

(20°,90°), and (10°,310°) at 2.55 $R_\odot$. At 4.50 $R_\odot$, the Michigan model density enhancements agree, in both value and location, with the tomographic density peaks near (25°,50°) and (−20°,200°). In contrast, the Stanford N_e values in the streamer belt at this height are somewhat higher than tomographic values (by up to a factor of 2 or so), and features are not so well aligned with the tomographic results. Note, however, that the Stanford model very clearly reproduces the low density regions near (20°,260°) at 2.55 and 4.50 $R_\odot$. Also at 4.50 $R_\odot$, the Stanford magnetic field contours capture the location of the low-density region near (20°,150°). All of these low-density features are less well reflected in the Michigan model.

Some of the quantitative comparisons described above can also be followed while inspecting Figures 5–8, which are described below. Those figures show specific regions selections at different heights as well as quantitative comparative analysis of the three model densities within the selected regions.

Figure 5 shows electron density color maps from the tomographic reconstruction (*right panels*), the Stanford model (*middle panels*), and the Michigan model (*left panels*). The top row of panels corresponds to 1.25 $R_\odot$, the middle row to 2.55 $R_\odot$, and the bottom row to 4.50 $R_\odot$. At each height (*rows*) the color scale is common through the three models (*columns*). At the different heights, the regions bounded by solid and dashed lines are used for the analysis presented in Figures 6–8. For all grid points within the boxes outlined with solid lines at each height, the top panels on top of Figures 6–8 show the scatter plots for the electron densities of each of the two MHD model densities compared against the tomographic values, and also for the MHD models against each other. At the top of each scatter plot we indicate the correlation coefficient[1] value among the compared densities. We also indicate the ratio of averages for the compared densities, in order to give an overall quantification of the similarity of the derived densities from the different models within the selected region.

Due to the lack of co-alignment of any given specific feature among the three models, the information provided by the scatter plots alone is not meaningful without the aid of plots explicitly showing density profiles as functions of longitude, latitude, and height. To that end, Figure 5 also contains horizontal and vertical dashed lines. The horizontal dashed lines indicate the range of latitudes for which the bottom left panels in Figures 6–8 display the averaged longitudinal profiles. In these plots the different line styles denote tomographic densities (*solid line*), Michigan (MI) model densities (*dashed line*), and Stanford (SU) model densities (*dot-dashed line*). Similarly, the vertical dashed lines in Figure 5 indicate the range longitudes for which the bottom middle panels in Figures 6–8 display the averaged latitudinal profiles, using the same line styles we just indicated above. Finally, the bottom right panels in Figures 6–8 display the averaged radial profiles (using the same line styles), averaged over all bins with latitudes and longitudes among the selected ranges (i.e., all bins within the dashed squares formed by the dashed line intersections).

At 1.25 $R_\odot$ (Fig. 6), the average profiles are representative of the southern hemisphere subpolar region. The scatter plot comparing the Stanford model and the tomographic results has the

[1] In each scatter plot, as a measure of the correlation between the model densities, we use the linear Pearson correlation coefficient $\rho_{x,y}$ between the *X*-axis and *Y*-axis density vectors.

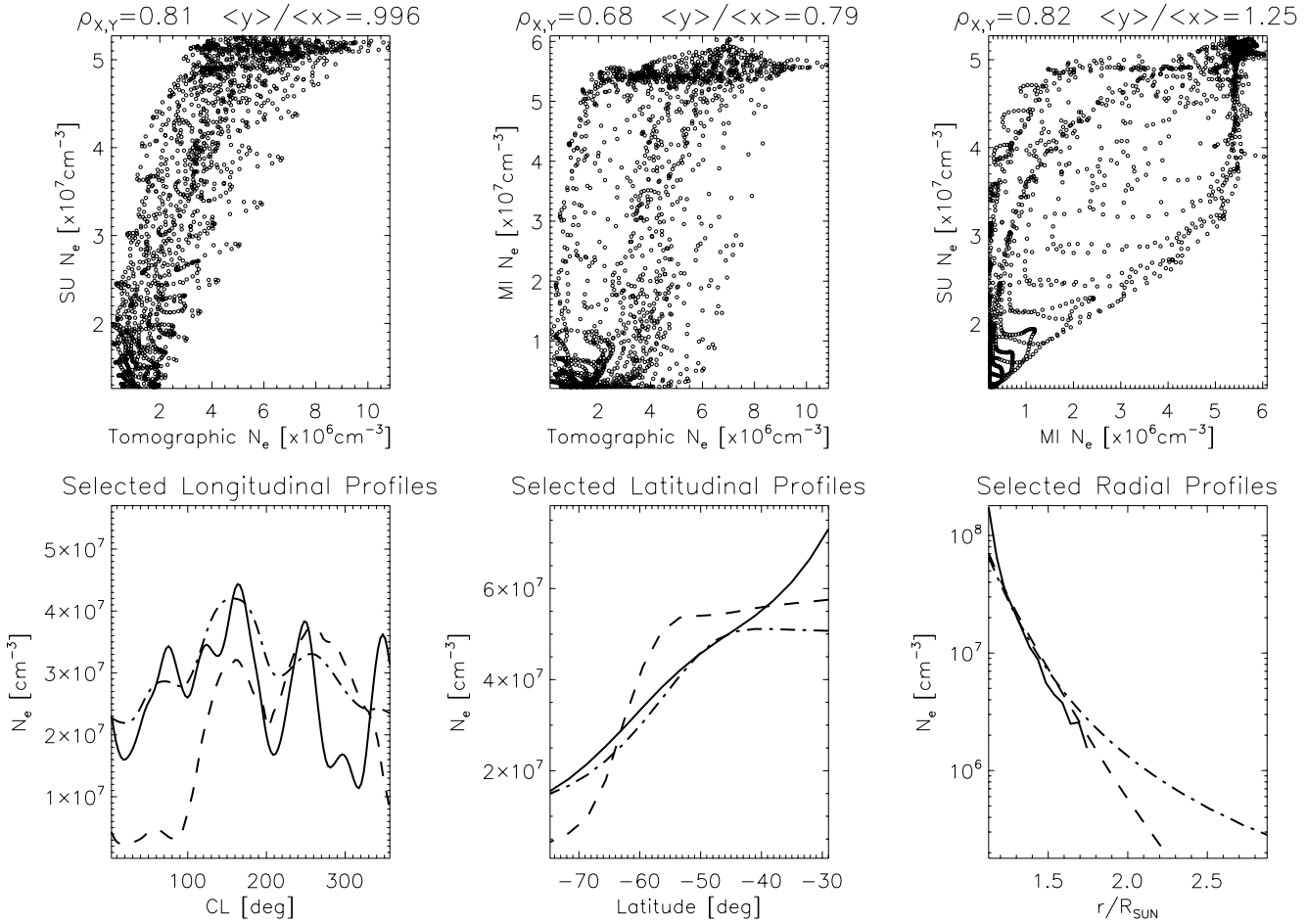

FIG. 6.— *Top*: Density scatter plots at 1.25 $R_\odot$ for the subpolar region boxed by the solid lines in the top row of Fig. 5, comparing the Michigan MHD (MI), Stanford MHD (SU), and tomographic models. *Bottom*: Average latitudinal, longitudinal, and radial density profiles, averages taken over the region bounded by the dashed lines in the top row of Fig. 5. *Solid lines*: tomography; *dashed lines*: Michigan; *dot-dashed lines*: Stanford.

highest correlation in this region. Consistently with this, the Stanford model profiles show more agreement with the tomographic results across all longitudes and latitudes within the analyzed region. The average subpolar radial profiles are very similar for all three models up to about 1.75 $R_\odot$.

At 2.55 $R_\odot$ (Fig. 7), the average profiles are representative of the streamer belt region. As can also be seen in the middle panels in Figure 4, the Michigan model reproduces more faithfully the average longitudinal and radial profiles of the tomographic result within the selected streamer belt region. This is also reflected in a higher correlation coefficient between this model's densities and those from the tomography. Similarly to the tomographic result, the average latitudinal profile of the Michigan model is singly peaked, while the Stanford model profiles show two maxima. In addition, the Michigan model streamer belt radial profiles reproduce the tomographic results more faithfully in this region.

At 4.50 $R_\odot$ (Fig. 8), the average profiles are representative of the streamer belt region. There is a good consistency of the average longitudinal profile of the Michigan model with the tomographic results. This was already noted out in reference to the bottom right panel in Figure 4, where we pointed out the alignment of the different maxima of the contour plots with the tomographic highest density regions along the streamer belt at that height. The selected radial profiles of both MHD models show a similar level of consistency with the tomographic results.

Similarly to the bottom right panels of Figures 6–8, Figure 9 shows, for both poles, the average density height profiles from the tomography and both MHD models. For each pole, the averages are taken over all longitudinal bins and the two latitudinal bins closest to each pole. The tomography results (*solid lines*) are shown in the respective instrument height ranges [1.10,1.75 $R_\odot$] for Mk IV and [2.35,5.00 $R_\odot$] for C2. Recently, the LASCO C2 pBs have been compared to those measured by the POISE eclipse expedition.[2] The comparison region ranged from 2.4 to 3.2 $R_\odot$, and excellent agreement was found, except over the north pole below 3.0 $R_\odot$. Below that height, the LASCO C2 pB values are too large by about 40%. This asymmetry in the LASCO polar values has also been noted by Frazin et al. (2002) in the comparison to the UVCS White Light Channel. Bearing that result in mind, one should consider the north polar/subpolar tomographic densities derived here as upper bounds for the underlying "real" values.

Consistent with the southern hemisphere subpolar comparison shown in Figure 6, the Stanford model shows good consistency with the tomographic densities in the south polar region (Fig. 9) in the Mk4 height range and within a factor of 2 or so in the C2 height range. Besides that, both MHD models show a very poor

[2] The LASCO POISE intercomparison, as well as other coronagraph intercalibration information can be found at http://secchi-ical.wikidot.com.

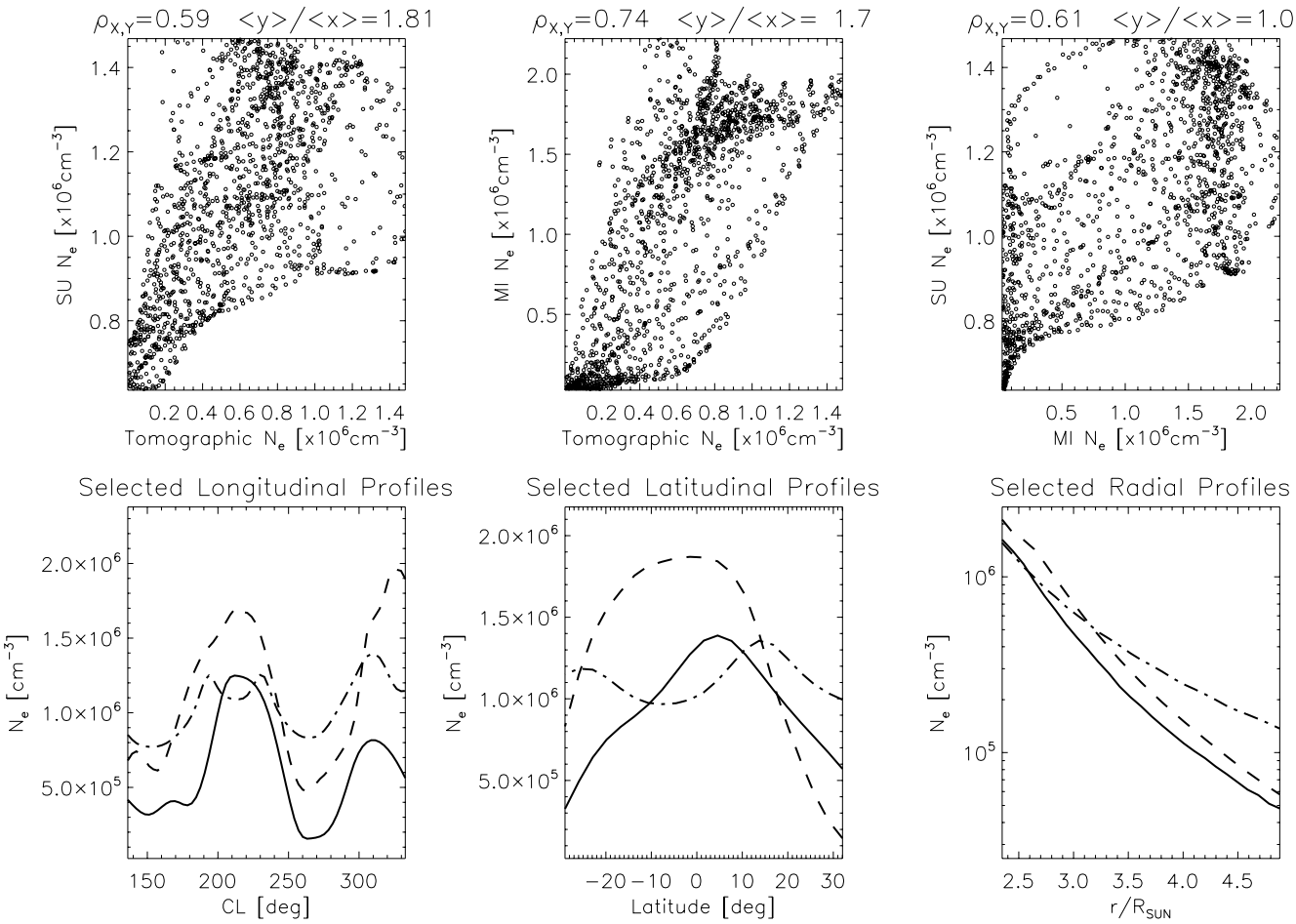

FIG. 7.—*Top*: Density scatter plots at 2.55 $R_\odot$ for the streamer belt region boxed by the solid lines in the middle row of Fig. 5, comparing the Michigan MHD (MI), Stanford MHD (SU), and tomographic models. *Bottom*: Average latitudinal, longitudinal, and radial density profiles, averages taken over the region bounded by the dashed lines in the middle row of Fig. 5. *Solid lines*: tomography; *dashed lines*: Michigan; *dot-dashed lines*: Stanford.

correspondence with the tomographic densities, far beyond any uncertainty attributable to the pB measurements.

3. DISCUSSION

Some of the differences in magnetic field morphology between the Stanford and Michigan models are due to the different order (N) used in the polynomial expansion of the magnetograms. Since the Stanford model uses $N = 9$ and the Michigan model uses $N = 90$, one might expect the Michigan model to resolve smaller scale structures. In the previous section, we found that the Michigan model neutral line is better co-aligned with the highest density features within the streamer belt. Despite this, we also noted that at higher latitudes the Stanford magnetic field morphology presents structures that correspond more directly to (enhanced and depleted) density features seen in the SRT maps. The fact that the Michigan model uses a Cartesian grid may be the cause for the partial lack of success in reproducing some structures seen in the tomography. A new spherical-grid version of the Michigan model is currently being validated. Although results are still preliminary, the new model more faithfully reproduces the morphological features seen in the SRT results.

In order to understand why the two models have somewhat different neutral line morphologies, note that in any MHD model, numerical resistivity causes the field lines near the current sheet to reconnect and form "V" shaped lines instead of a more realistic stretched form. In order to avoid this problem, the Michigan model refines the grid near the current sheet to obtain the necessary spatial resolution in that region (Cohen et al. 2007a). In addition, the model also uses the less diffusive, nonlinear Roe solver based numerical scheme (see Sokolov et al. 2007) to avoid the reconnection. Both numerical models employ the total variation diminishing (TVD) MUSCL approach, to achieve second-order accuracy (about the Stanford model, see Hayashi 2005). An important difference between the two models is that the Stanford model does not make use of grid refinement. This may result in wider closed field regions and a lower maximum density within them. However, the Cartesian grid used in the Michigan model may cause some problems with representing the lower boundary conditions. These issues will be better addressed by the new spherical-grid Michigan model, and we will provide new comparisons of its results against tomographic inversions in a future work.

From the present work, it is clear that there is no simple characterization of the comparison between the tomographic reconstructions and the Michigan and Stanford models, except that both models have a major problem reproducing polar densities. As pointed out in § 2, there is a lack of co-alignment in the coronal features (density enhancements, low-density regions, etc.) shown by the different results. Beyond intrinsic differences among the various models' implementations, one possible cause for the observed differences among their results is coronal dynamics, as well as time shifting among the observational periods of the various data sets used by the different reconstructions and models. For the same reasons, the reproduced coronal structures exhibit shape and size differences. These issues must be taken

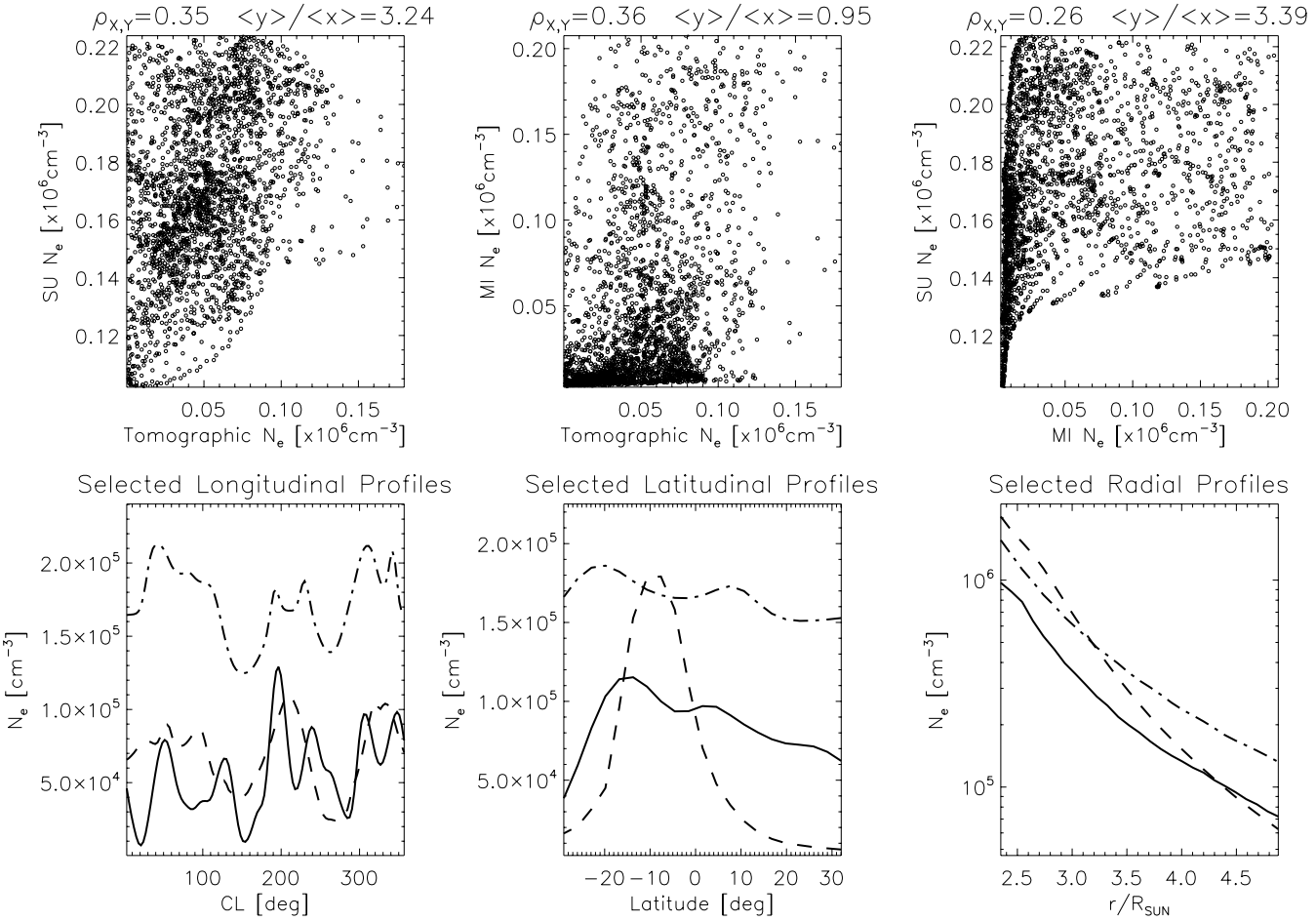

FIG. 8.— *Top*: Density scatter plots at 4.50 $R_\odot$ for the streamer belt region boxed by the solid lines in the bottom row of Fig. 5, comparing the Michigan MHD (MI), Stanford MHD (SU), and tomographic models. *Bottom*: Average latitudinal, longitudinal, and radial density profiles, averages taken over the region bounded by the dashed lines in the bottom row of Fig. 5. *Solid lines*: tomography; *dashed lines*: Michigan; *dot-dashed lines*: Stanford.

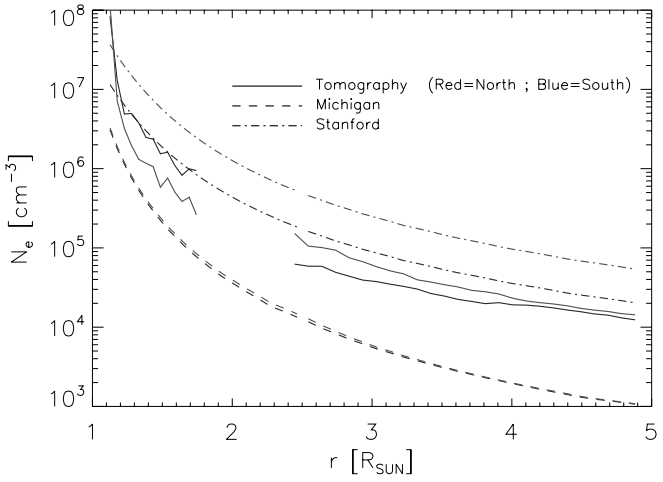

FIG. 9.—Average polar density profiles from the tomography and both MHD models. For each pole, the averages are taken over all longitudinal bins and the two latitudinal bins closer to the pole. The tomography results derived from Mk IV data are shown in the heliocentric height range [1.0, 1.75 $R_\odot$], and those derived from C2 data are shown in the range [2.35, 5.00 $R_\odot$]. [*See the electronic edition of the Journal for a color version of this figure.*]

into account when comparing MHD models and tomographic reconstructions.

In taking the tomographic reconstruction as a reference against which the models are to be compared, it must be considered that there is a time resolution limit for the features that may be reliably recovered by static SRT. This is also due to coronal dynamics and the necessary time lapse to gather the required data, which is about 14 days for density reconstructions based on single-point-of-view pB data. Thanks to the new *STEREO* mission and the continuation of *SOHO*, it has become possible to simultaneously observe the solar corona from three different points of view. In this situation, the time required to collect the necessary data may be dramatically reduced by up to a factor of order 3 during periods of close-to-optimal spacecraft angular separation. We are currently further developing our tomographic codes to be able to handle simultaneously collected data from MLSO Mk IV, *SOHO* C2, and *STEREO* SECCHI.

Considering the preceding discussion, a main conclusion from this work is then that global comparisons of MHD models against static-SRT results are not straightforward. Instead, comparisons made within regions specifically selected from the period under consideration are a better approach. The more relevant and stable coronal features should first be recognized in the time series observations used for the tomographic reconstructions, such as the polar, subpolar, and streamer-belt regions selected for analysis in this paper. The global properties of these regions as observed in the tomographic reconstructions, such as the averaged density

profiles indicated by solid lines in Figures 6–9, provide then reliable and useful average constraints for the same regions in the proposed MHD models.

As a general remark from the comparisons shown in this work, we find that the presented MHD models have in general a better morphological agreement with the tomographic densities in the region below 3.5 $R_\odot$. At larger heights the agreement is more problematic. Given the observed differences in density values between the tomography and the models at the lowest height range (top panels in Fig. 4), our interpretation is that the base densities and temperatures of the models need to be improved. In addition, the radial profile analysis for different regions (bottom right panels in Figs. 6–8, and Fig. 9), suggests that the height gradients of the models need further adjustments.

The SRT reconstructed densities reach down to 1.1 $R_\odot$, providing a direct constraint on the MHD models down to that height. At these lower heights, where the advective acceleration term $(\boldsymbol{v} \cdot \nabla \boldsymbol{v})$ is negligible, the model densities are essentially controlled by the temperature through the hydrostatic scale height. It should be noted, however, that density scale-height enhancements may occur in presence of MHD waves. As proposed by Litwin & Rosner (1998), waves may exert a ponderomotive force on a plasma that opposes gravity, leading to an extended pressure scale height. The models presented here do not account for wave pressure gradients, and this issue is out of the scope of this paper. In any event, model agreement at these lower heights can be improved by adjusting the temperature at the coronal base as a function of latitude and longitude, as well as adjusting the base densities. In the Michigan model, adjusting the base temperature requires adjustment of the polytropic index to avoid having an effect on the solar wind at large distances (Cohen et al. 2007b). We note that the Michigan model is designed to faithfully reproduce the solar wind flow along the open field lines and does not attempt to correctly represent the plasma in the closed-field structures such as helmet streamers, which have hydrostatic solutions. The Stanford model makes use of a constant polytropic index, for an adiabatic expansion. A first effort of the Stanford model to improve the MHD global model using a non-uniform coronal base boundary condition on the temperature can be found in Hayashi et al. (2006). In that work the temperature map was derived from the multiwavelength observations by the EIT on *SOHO*. However, the interpretation of EUV images in terms of temperatures is complicated and not unique (e.g., Schmelz et al. 2007; Frazin et al. 2005b).

The tomographic technique can be extended to the EUV and X-ray ranges, in such a way that a temporal series of observations in different bandpasses (e.g., EIT, EUVI, XRT, AIA) could eventually lead to 3D electron temperature (more precisely, differential emission measure) maps (Frazin et al. 2005b). We have already given preliminary results on EUV tomography based on EIT series of observations in 171, 195, and 284 A (Frazin et al. 2007a). We are currently working on EUV tomography, and we will present the results in a future article. Combined multiwavelength tomography and MHD coronal modeling efforts could then provide direct constraints to be matched by both the densities and electron temperatures of MHD models. Furthermore, a procedure called data assimilation has the potential to produce MHD simulations that agree with white-light and EUV observations in a manner that is akin to terrestrial weather prediction (e.g., Ghil 1989; Frazin et al. 2005a).

This research was supported by the NSF SHINE and CMG programs, awards 0555561 and 0620550, respectively, to the University of Illinois. A. M. V. acknowledges the CONICET grant PIP 6220 to IAFE for partial support. We wish to thank the anonymous referee for his/her suggestions, which improved the manuscript.

REFERENCES

Altschuler, M. D., & Perry, R. M. 1972, Sol. Phys., 23, 410
Arge, C. N., Odstrcil, D., Pizzo, V. J., & Mayer, L. R. 2003, in AIP Conf. Proc. 679, 10th International Solar Wind Conference, ed. M. Velli, R. Bruno, & F. Malara (Melville: AIP), 190
Arge, C. N., et al. 2004, J. Atmos. Solar-Terr. Phys., 66, 1295
Cohen, O., Sokolov, I. V., Roussev, I. I., & Gombosi, T. I. 2007a, J. Geophys. Res., 113, A03104
Cohen, O., et al. 2007b, ApJ, 654, L163
Elmore, D. F., Burkepile, J. T., Darnell, J. A., Lecsinki, A. R., & Stanger, A. L. 2003, Proc. SPIE, 4843, 66
Frazin, R. A. 2000, ApJ, 530, 1026
Frazin, R. A., Butala, M. D., Kemball, A., & Kamalabadi, F. 2005a, ApJ, 635, L197
Frazin, R. A., & Janzen, P. 2002, ApJ, 570, 408
Frazin, R. A., & Kamalabadi, F. 2005, Sol. Phys., 228, 219
Frazin, R. A., Kamalabadi, F., & Weber, M. A. 2005b, ApJ, 628, 1070
Frazin, R. A., Vásquez, A., & Kamalabadi, F. 2007a, AGU Abstr. Fall, SH23A1060F
Frazin, R. A., Vásquez, A. M., Kamalabadi, F., & Park, H. 2007b, ApJ, 671, L201
Frazin, R. A., et al. 2002, in Radiometric Calibration of *SOHO*, ISSI Scientific Report SR-002, ed. A Pauluhn, M. C. E. Huber, & R. von Steiger (Noordwijk: ESA), 249
Ghil, M. 1989, Dyn. Atmos. Oceans, 13, 171
Hayashi, K. 2005, ApJS, 161, 480
Hayashi, K., Benevolenskaya, E., Hoeksema, T., Liu, Y., & Pu Zhao, X. 2006, ApJ, 636, L165
Litwin, C., & Rosner, R. 1998, ApJ, 506, L143
Lugaz, N., Manchester, W. B., IV, & Gombosi, T. I. 2005, ApJ, 627, 1019
Manchester, W., IV 2005, ApJ, 622, 1225
Manchester, W., IV, Gombosi, T., Ridley, A., Roussev, I., DeZeeuw, D. L., Sokolov, I., Powell, K., & Toth, G. 2004, J. Geophys. Res., 109, A02107
Manchester, W. B., IV, et al. 2005, ApJ, 622, 1225
Mancuso, S., & Raymond, J. C. 2004, A&A, 413, 363
Moran, T. G., et al. 2006, Sol. Phys., 237, 211
Morgan, H., Habbal, S. R., & Woo, R. 2006, Sol. Phys., 236, 263
Odstrcil, D., Linker, J., Lionello, R., Mikić, Z., Riley, P., Pizzo, V., & Luhmann, J. 2002, J. Geophys. Res., 107, 1493
Odstrcil, D., & Pizzo, V. J. 1999, J. Geophys. Res., 104, 493
Reames, D. V. 1999, Space Sci. Rev., 90, 413
Riley, P., Linker, J. A., & Mikić, Z. 2001, J. Geophys. Res., 106, 15889
Schmelz, J. T., Kashyap, V. L., & Weber, M. A. 2007, ApJ, 660, L157
Sokolov, I. V. 2004, ApJ, 616, L171
Sokolov, K. G., Powell, I. I., Cohen, O., & Gombosi, T. I. 2007, ASP Conf. Ser. 385, Numerical Modeling of Space Plasma Flows, ed. N. V. Pogorelov, E. Audit, & G. P. Zank (San Francisco:ASP), 291
Wang, Y.-M., & Sheeley, N. R. 1990, ApJ, 355, 726
Yurchyshyn, V., Liu, C., Abramenko, V., & Krall, J. 2006, Sol. Phys., 239, 317